

The Near-Infrared Discrete Extinction Laws of the Galactic Center

DEVAL M. DELIWALA¹ AND MATTHEW W. HOSEK JR.²

¹Department of Mathematics, University of California, Berkeley

²Department of Physics and Astronomy, University of California, Los Angeles

ABSTRACT

A precise spatially resolved extinction law is essential for interpreting observations of the highly reddened Galactic Center (GC). We analyze 21,195 red-clump (RC) stars in the *James Webb Space Telescope* NIRCam mosaic of the central $120'' \times 120''$ (avg. $A_{Ks} \sim 2.5\text{mag}$) in the near-infrared ($\sim 1.15 - 4.05\mu\text{m}$) regime. Treating each of the four detector footprints (NRCB1–4) as an independent sightline, we fit the RC ridge line in the F115W, F212N, F323N, and F405N color-magnitude diagrams with an iterative MCMC routine that models the RC as many compound Gaussian + linear backgrounds, and convert the fitted slopes into extinction ratios relative to F212N. The extinction laws diverge at short wavelengths between footprints; NRCB3 ($A_{F115W}/A_{F212N} = 3.65 \pm 0.11$) exceeds NRCB4 (3.25 ± 0.07) by $> 3\sigma$, while the longer-wavelength ratios cluster more tightly and are statistically insignificant: ($A_{F323N}/A_{F212N} = 0.58 - 0.67$ and $A_{F405N}/A_{F212N} = 0.36 - 0.41$). Relative to Fritz et al. (2011), our measurements agree to within 1% for NRCB1 and NRCB3 but are flatter by 9% (NRCB2) and 10.5% (NRCB4) at F115W, hinting at $\sim 5\text{pc}^2$ variations in dust properties across the $\sim 22\text{pc}^2$ observation field. These spatial differences, which are $0.05 - 3.19\sigma$ at F115W ($\sim 1.15\mu\text{m}$) yet $< 1\sigma$ beyond $3\mu\text{m}$, demonstrate that even within the GC, adopting region-specific ratios is necessary for precision studies of GC stellar populations.

1. INTRODUCTION

Understanding how interstellar dust dims and reddens starlight is essential for every area of Galactic and extragalactic astronomy. Distance estimates based on standard candles (Freedman et al. 2001), stellar mass functions in embedded clusters (Lada & Lada 2003), and large-scale maps of the Milky Way (Green et al. 2015) all depend on accurate corrections for wavelength-dependent attenuation. *Extinction* is the combined absorption and scattering of light along the line of sight, and an *extinction law* describes how the extinction magnitude, A_λ , varies with wavelength.

Early work from the optical to the near-infrared (OIR; $0.8\mu\text{m} \lesssim \lambda \lesssim 2.2\mu\text{m}$) showed that A_λ could be approximated by a single power law, $A_\lambda \propto \lambda^{-\beta}$, with β ranging from $\approx 1.5 - 1.8$ based on modest photometric samples (Rieke & Lebofsky 1985; Draine 1989; Cardelli et al. 1989; Martin & Whittet 1990; Fitzpatrick 1999). This “universal” power law form in the OIR became standard for many years. However, Martin & Whittet (1990) did foreshadow that it would be “remarkable” for a single power-law to be appropriate over an extended wavelength range.

Large surveys have since shown that even in the near-infrared (NIR; $1.15\mu\text{m} \lesssim \lambda \lesssim 4.05\mu\text{m}$), the extinction curve departs from a simple power law. Using 2MASS

photometry, Froebrich et al. (2007) demonstrated that β systematically decreases toward lower Galactic latitudes. Later, Fitzpatrick & Massa (2009) leveraged the well determined distance d to the young cluster NGC 6530 to compute $R(V) = A(V)/E(B - V)$ directly from d and the cluster’s absolute magnitude, finding $5.2 \leq R(V) \leq 6.1$. This is substantially lower than the $R(V) \approx 7.0$ inferred by extrapolating a β -power law fit. These variations prompted both empirical and physical models. Fitzpatrick & Massa (2009), using 2MASS and the Advanced Camera for Surveys (ACS) aboard the *Hubble Space Telescope* (HST), introduced a two-parameter analytic model that allows a steepening blueward of $1\mu\text{m}$. Schlafly et al. (2016) used APOGEE spectroscopy with 2MASS photometry to show that optical-mid-IR extinction is well described by a one-parameter family of curves parameterized by $R(V)$, with only modest line of sight variations. Models that adopt a size distribution, with larger grains concentrated in dense clouds and smaller grains in the diffuse ISM, also successfully reproduce the bulk of the observed extinction variations (Weingartner & Draine 2001). Composite models combining fresh silicates near the Galactic Center (GC) with foreground screens naturally produce curves steeper or flatter than the diffuse-

Milky Way baseline, depending on the small/large grain ratio (Gao et al. 2013; Voshchinnikov et al. 2017).

However, survey-driven studies face two major issues. First, depth limits cause highly-reddened stars to drop below detection thresholds, so bulk fits are dominated by less-reddened foreground stars (e.g., Schultheis et al. 2009). Second, coarse resolution ($\gtrsim 1''$) blends sources in crowded regions, skewing colors where extinction is greatest (e.g., Nogueras-Lara et al. 2021). Both effects are most severe at the GC, where $A_{Ks} \simeq 2.5$ on average and stellar densities exceed 10^7 stars deg $^{-2}$ (e.g., Schödel et al. 2010; Nogueras-Lara et al. 2019).

Consequently, high-resolution, targeted approaches have been pivotal for Galactic Center extinction studies. ISO-SWS and VLT/SINFONI spectroscopy of hydrogen recombination lines in the minispiral (a bright HII region within the central 20'') yield a NIR power law index of $\beta = 2.11 \pm 0.06$ for $\lambda \lesssim 2.8 \mu\text{m}$ (Fritz et al. 2011). Similarly, *HST*/WFC3-IR photometry of 819 red-clump (RC) giants in the GC, combined with 453 proper-motion-selected main-sequence stars in Westerlund 1, reveals an extinction curve both steeper than the diffuse-ISM law and also inconsistent with a single- β power law across the NIR (Hosek et al. 2018, 2019). Also, using high proper-motion stars, Haggard et al. (2024) found a relative L' -band ($\simeq 3.80 \mu\text{m}$) extinction significantly higher than previous studies, which they attribute to stars moving through grain populations local to the GC different from those along the line-of-sight.

JWST has further advanced the field. NIRCam provides 0.031'' resolution in its short-wavelength channels and an exceptional sensitivity to faint, reddened stars (e.g., Schödel et al. 2025). Early JWST extinction-law results outside the GC already demonstrate its potential: RC measurements in 30 Doradus have total-to-selective extinction ratios $A_\lambda/E(F090W - F200W)$ twice the diffuse-MW law beyond 1 μm (Fahrion et al. 2023); pair-matched NIRSpec spectra behind Westerlund 2 show a near-IR slope range $1.5 \leq \beta \leq 2.4$ with filter-specific coefficients (Wang et al. 2024); and color-excess ratios in the Pillars of Creation flatten from $\beta \approx 2.4$ at 1 μm , to $\beta \approx 1.6$ at 4 μm (Li et al. 2024).

In this context, JWST/NIRCam photometry of the central 120'' \times 120'' of the GC provides useful photometry. Four detector footprints (NRCB1-4, see Figure 1) cover $\sim 5.4 \text{pc}^2$ tiles at 8kpc, enabling direct tests of spatial variation on parsec scales. Observations in F115W, F212N, F323N, and F405N span $\simeq 1.15 \mu\text{m} - 4.05 \mu\text{m}$, covering the regime where ice features, grain growth, and radiative-transfer effects shape the extinction curve (e.g., Boogert et al. 2015).

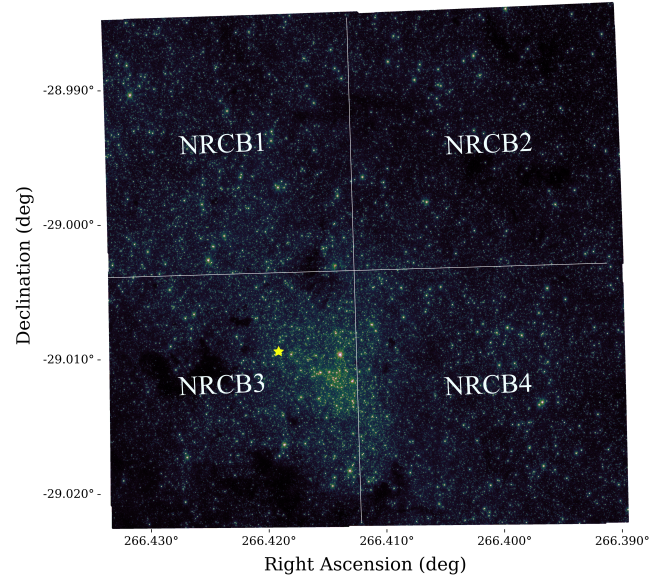


Figure 1. JWST NRCB region coverage. The yellow star indicates Sagittarius A*.

One of the foundational methods of deriving the extinction law is the “Red Clump (RC) method,” introduced by Wozniak & Stanek (1996). RC stars are a population of evolved stars in their core-helium burning phase. Their helium-core masses are nearly identical, and in the K-band, their absolute magnitudes depend only on metallicity and age (e.g., Khan et al. 2023). Thus, RC stars serve as reliable infrared standard candles. Assuming a uniform intrinsic color, any color spread on a color-magnitude diagram (CMD) arises primarily from interstellar extinction. As a result, RC stars are also excellent extinction probes (Gao et al. 2009; Girardi 2016). By analyzing the mean magnitudes and colors of red giant stars (often RC) across different wavelength bands, Messineo et al. (2005); Nishiyama et al. (2009) reported steeper extinctions of $\beta = 1.9$ and 2.0 respectively towards the Galactic Bulge.

This work uses the RC method on these JWST NRCB1-4 catalogs to (i) measure absolute extinction ratios A_λ/A_{F212N} in each footprint, (ii) assess statistical differences between tiles, and (iii) compare our results to existing GC laws (e.g., Nishiyama et al. 2009; Fritz et al. 2011; Hosek et al. 2019; Nogueras-Lara et al. 2020; Haggard et al. 2024). Section 2 outlines the data, Section 3 describes the methodology for measuring A_λ/A_{Ks} extinction ratios, Section 4 presents our results, Section 5 compares our results to known GC laws, and finally, Section 6 summarizes our work.

2. OBSERVATIONS AND MEASUREMENTS

3. METHODS

In a color-magnitude diagram (CMD) the RC cluster appears as a narrow, tilted “bar” at short wavelengths ($\sim 1 - 2\mu\text{m}$), because every star (roughly) shares the same intrinsic magnitude M_λ and color. The *observed* shifts of those stars are thus driven almost entirely by extinction. Let the two filters be λ_B (bluer) and λ_R (redder). If the bluer magnitude m_{λ_B} is placed on the vertical axis and the color $m_{\lambda_B} - m_{\lambda_R}$ on the horizontal axis, a linear regression of the RC ridge gives the total-to-selective extinction ratio

$$R_{\lambda_B} = \frac{A_{\lambda_B}}{E_{\lambda_B - \lambda_R}} = \frac{\partial m_{\lambda_B}}{\partial(m_{\lambda_B} - m_{\lambda_R})}.$$

Repeating the fit with the redder m_{λ_R} filter on the vertical axis against the same color yields

$$R_{\lambda_R} = \frac{A_{\lambda_R}}{E_{\lambda_B - \lambda_R}} = \frac{\partial m_{\lambda_R}}{\partial(m_{\lambda_B} - m_{\lambda_R})}.$$

Because both regressions share the same color excess $E_{\lambda_B - \lambda_R} \simeq A_{\lambda_B} - A_{\lambda_R}$ (for RC stars), geometry forces the two slopes to differ by one.

$$R_{\lambda_B} - R_{\lambda_R} = \frac{A_{\lambda_B}}{A_{\lambda_B} - A_{\lambda_R}} - \frac{A_{\lambda_R}}{A_{\lambda_B} - A_{\lambda_R}} = 1. \quad (1)$$

Hence, measuring any single RC slope fixes the other ($R_{\lambda_B} = R_{\lambda_R} + 1$), and their ratio yields the ratio of total extinction:

$$\frac{A_{\lambda_B}}{A_{\lambda_R}} = \frac{R_{\lambda_B}}{R_{\lambda_R}} = \frac{R_{\lambda_R} + 1}{R_{\lambda_R}}. \quad (2)$$

Therefore, measuring the ratio of total extinction $A_{\lambda_B}/A_{\lambda_R}$ reduces to a linear regression and trivial division, a direct consequence of RC geometry in CMD space. A_λ/A_{F212N} is derived for $\lambda \in \{F115W, F323N, F405N\}$. Three slope measurements are required for every NRCB1-4 footprint. For simplicity, the procedure for NRCB1 is described. The same steps apply to NRCB2-4.

3.1. Extracting the Red Clump

The RC is first isolated from the surrounding stellar population. To do this, the large extinction difference between F115W and F212N ($A_{F115W}/A_{F212N} \approx 3.63$, Fritz et al. (2011)) is exploited. This makes the RC bar steep and well-defined in the F115W - F212N vs. F115W CMD. To minimize outliers while ensuring ample RC coverage, the unsharp-masking technique described in De Marchi et al. (2016) is used. The CMD is first converted to a Hess Diagram, which represents stellar density as a 2D histogram. Each star’s position is modeled as a normal distribution, with its width determined from the associated photometric error. The histogram is

built with a bin size of 0.02 mags in both color (F115W - F212N) and magnitude (F115W) space. To generate the unsharp mask, the Hess Diagram is convolved with a 2D Gaussian Kernel of 0.3 mag width. The convolved Hess Diagram is then subtracted from the original. Finally, a power-law (gamma) normalization with exponent $\gamma = 1.5$ is applied using Matplotlib’s `PowerNorm` transform. Concretely, each pixel intensity I transforms as

$$I' = \left(\frac{I - I_{\min}}{I_{\max} - I_{\min}} \right)^{\gamma=1.5},$$

which further enhances the contrast of the RC bar relative to the surrounding background. The resulting unsharp mask for NRCB1 F115W - F212N vs. F115W is shown on the right of Figure 2. Afterwards a tight parallel cutoff was defined by-eye that encloses the RC bar, which is expanded by a factor of three to ensure sufficient coverage (a ~ 2.4 mag vertical RC width for F115W-F212N vs. F115W). This is only a conservative ansatz, which is improved by the algorithm described in Sections 3.2.1 and A.

5,027 stars are selected in NRCB1 that lie within the expanded blue boundaries and matched to the redder F323N and F405N catalogs. Specifically, the RC is sampled once in the high-contrast F115W–F212N CMD – where it is morphologically well defined in the Hess diagram – and the same selection is “lifted” to all redder filter CMDs. At longer wavelengths (e.g. F212N–F323N or F323N–F405N), the absolute extinction differences

$$\Delta A = A_{\text{bluer}} - A_{\text{redder}} \quad (3)$$

become smaller (e.g. $\Delta A_{F212N-F323N} < \Delta A_{F115W-F212N}$), so the RC ridge is increasingly washed out. By anchoring the selection in the F115W–F212N CMD (where ΔA is large and the clump is sharpest; see Figure 7), a consistent sample is maintained without having to redefine the RC in each subsequent CMD. 3237, 6544, 6387 RC stars were likewise selected in NRCB2-4 respectively (Table 1).

3.2. RC Ridge Curve Fitting Algorithm

Now that the RC population is isolated across F115W–F405N, straight lines are fit to the RC ridge in three CMDs:

- F115W – F212N vs. F115W
- F115W – F323N vs. F115W
- F115W – F405N vs. F115W

Similar to the selection of the RC population via the F115W–F212N CMDs in each region, the RC ridge is fit

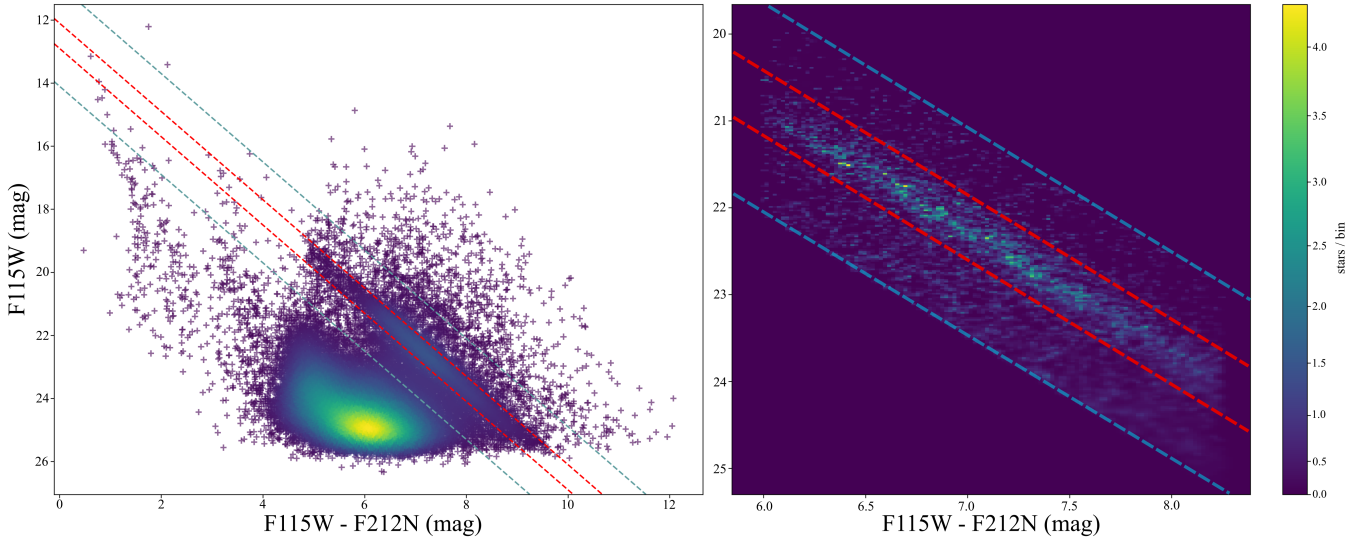


Figure 2. Selection of RC stars in NRCB1. Following De Marchi et al. (2016), the observed CMD (left panel) is converted into a Hess diagram and unsharp masking is applied to isolate the high-density RC ridge; initial by-eye boundaries (red lines) are then drawn around this feature and expanded by a factor of three (blue lines) to ensure comprehensive RC star coverage.

Table 1. Number of RC selected for each NRCB footprint.

Footprint	Total # stars ^a	# RC stars selected $\forall \lambda$
NRCB1	50,288	5,027
NRCB2	56,101	3,237
NRCB3	51,396	6,544
NRCB4	49,322	6,387

^aFrom photometry in the F212N filter. Different filters have different star counts in each footprint. The RC stars are matched across all λ .

using $F115W - \lambda$ CMDs because the extinction differential (Equation 3) increases at longer wavelengths relative to $F115W$. Consequently, the RC is more prominent in these CMDs, yielding tighter constraints on the slope. The ratio

$$\frac{A_{F115W}}{E(F115W - \lambda)}$$

is first calculated in each $F115W - \lambda$ CMD, and converted to A_λ/A_{F115W} using Equations 1 and 2. Then

$$\frac{A_\lambda}{A_{F115W}} \Rightarrow \frac{A_\lambda}{A_{F212N}}$$

are algebraically derived for all filters $F115W$, $F212N$ (equal to 1), $F323N$, and $F405N$.

The choice of $F115W$ on the y -axis is partly arbitrary, but it lies closer to the spectral energy-distribution peak of red-clump giants ($T_{\text{eff}} \sim 4800$ K, $\lambda_{\text{max}} \sim 0.6\mu\text{m}$), so

RC stars are intrinsically brighter in that band. In practice the tightening of the clump locus is marginal, but anchoring all CMDs on the same y -axis should translate into slightly smaller uncertainties on the final fitted extinction-law slopes. However, the exact choice is not critical: as shown in Equation 1, measuring the slope in one projection fixes the slope in the complementary CMD by a difference of one.

The CMDs fall into two categories: *those with a high-contrast RC bar and those without*. Most of the CMDs belong in category 1, with crisp RC bars, but the $F115W - F323N$ vs. $F115W$ diagrams in all NRCB footprints belong to category 2, with a slightly more broad RC feature (see the top-right figures in Figure 4–15). To handle both cases, we adopt two slope measurement methods: Method 1 is applied to every CMD, while Method 2, described in the appendix, although less precise, serves to verify Method 1’s slope measurements from the $F115W - F323N$ vs. $F115W$ CMDs.

3.2.1. Method 1

The procedure begins by dividing the RC bar into $n = 10$ contiguous tiles. Within each tile a compound Gaussian + Linear model is fit to the vertical density distribution using MCMC. The Gaussian component captures the RC overdensity while the linear component describes the background trend. After extracting the mean magnitude from the Gaussian fit in each tile, a linear regression is performed through the $n = 10$ mean magnitudes to calculate the overall RC slope.

The tiles must lie *orthogonal* to the RC ridge so that the MCMC-derived means trace the ridge itself for the

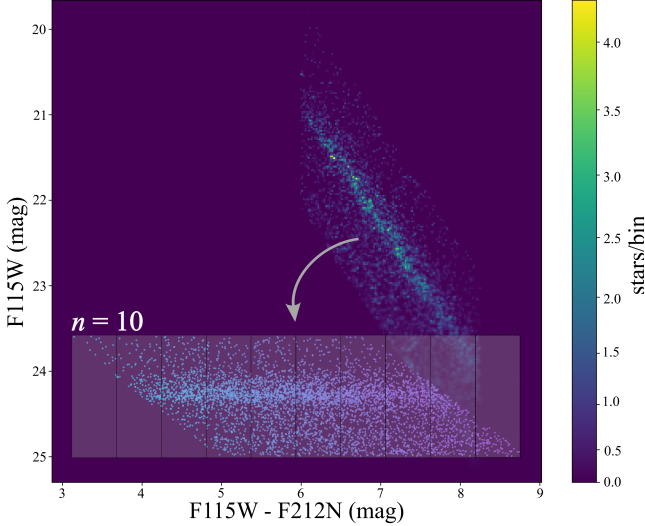


Figure 3. Method 1 – Tiles are generated along the RC bar to guide the collective MCMC slope fit: the CMD is first rotated by an angle $\theta = \tan^{-1}(m_{\text{ansatz}})$ to horizontalize the RC ridge, then $n = 10$ vertical bins are placed across this rotated ridge, and MCMC is used to fit a compound Gaussian + linear model in each tile (Figure 4).

Input: RC region, number of tiles n .

Output: Slope $m \pm \sigma_m$

Partition the RC color range into n tiles $\{T_{k=1}^n\}$.

for $k \leftarrow 1$ **to** n **do**

$S_k \leftarrow$ stars with colors in tile T_k .
 Fit a Gaussian + linear model to S_k via MCMC.
 Record the RC mean magnitude μ_k .
 Set $x_k \leftarrow$ color coordinate of center of T_k .

end

Form the set of points $\{x_k, \mu_k\}_{k=1}^n$.

$m, \sigma_m \leftarrow$ weighted linear fit through $\{x_k, \mu_k\}$.

return m, σ_m

Method 1: Measuring the RC Slope.

final linear regression. Otherwise each returned mean would be skewed with the geometric tilt of its tile. To accomplish this, the CMD is rotated counter-clockwise by $\theta = \tan^{-1}(m_{\text{ansatz}})$ where m_{ansatz} is the slope of the provisional parallel cutoffs defined in Section 3.1:

$$\begin{pmatrix} x_{\text{rot}} \\ y_{\text{rot}} \end{pmatrix} = \begin{pmatrix} \cos \theta & -\sin \theta \\ \sin \theta & \cos \theta \end{pmatrix} \begin{pmatrix} x \\ y \end{pmatrix} = \hat{R} \begin{pmatrix} x \\ y \end{pmatrix}.$$

where x is the color F115W- λ and y is the F115W RC magnitudes. This rotation renders the RC bar (roughly) horizontal. n vertical, contiguous tiles are laid across the full length of the horizontal bar. In this frame, the tiles are now orthogonal to the RC ridge. This process is

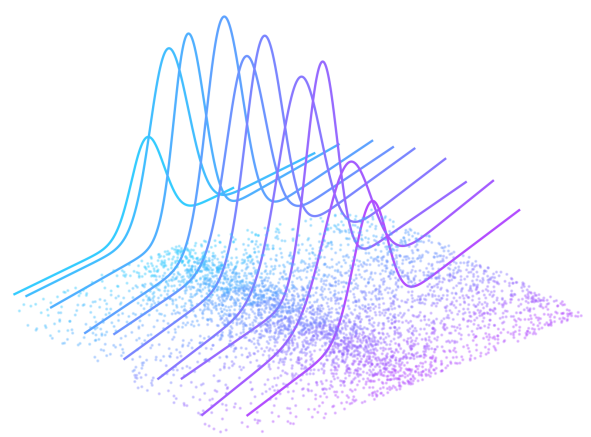


Figure 4. Three-dimensional view of the NRCB1 red clump ridge analysis with $n = 10$ tiles. The fitted Gaussian means from each tile trace out the RC ridge in this rotated frame.

visualized in Figure 3. A choice of $n = 10$ was made and is justified in Section 3.3.

Within each tile, the compound fit to the 1D distribution of y_{rot} is performed, treating it as a sum of a narrow Gaussian bump (RC stars) and a gentle varying continuum (everything else). This rotation ensures the returned Gaussian mean magnitudes from each tile follows the RC bar itself without any geometric skew.

Mixture Model—For a single histogram bin center y_i (after rotation), with observed count n_i and Poisson error $\sigma_i = \sqrt{n_i + 1}$, the following intensity model is posited.

$$\lambda(y_i|\vec{\theta}) = A \exp \left[-\frac{1}{2} \left(\frac{y_i - \mu}{\sigma} \right)^2 \right] + (1 - f_{\text{RC}})(my_i + b),$$

with parameter vector

$$\vec{\theta} = (u, A, \mu, \sigma, m, b), \quad f_{\text{RC}} = \frac{1}{1 + e^{-u}} \in (0, 1).$$

where

- A, μ, σ describe the Gaussian-component RC peak.
- m, b describe the Linear-component non-RC continuum.
- f_{RC} physically represents the *fraction* of all stars in the tile that belong to the RC component. The logit, $u \in \mathbb{R}$, is sampled rather than f_{RC} itself, so that walker diffusion is unrestricted, instead of sampling a fraction in $[0, 1]$. This also reduces the integrated autocorrelation time described in Section 3.3.

Assuming independent Gaussian noise, the log-likelihood for one tile is

$$\ln \mathcal{L} = -\frac{1}{2} \sum_i \left[n_i - \lambda(y_i | \vec{\theta}) \right]^2 / \sigma_i^2 - \frac{1}{2} \sum_i \ln(2\pi\sigma_i^2).$$

Priors—Weakly informative but physically motivated priors are imposed:

$$\begin{aligned} u &\sim \text{logit-Beta}(\alpha = 3, \beta = 2), \\ A &\sim \mathcal{U}(0, 10^3), \\ \mu &\sim \mathcal{U}(\bar{y} - 2s, \bar{y} + 2s), \\ \sigma &\sim \mathcal{U}(\max\{0, s - 0.5\}, s + 0.5), \\ m &\sim \mathcal{U}(-\infty, 30), \quad b \sim \mathcal{U}(-\infty, 50), \end{aligned}$$

where \bar{y} and s are the sample mean and standard deviation of y_{rot} . Priors are zero outside the stated intervals, so the overall log-prior is $-\infty$ whenever a walker steps outside these bounds. The values $\alpha = 3, \beta = 2$ reflect the expectation that, within a well-selected tile, a majority of stars may be RC. However, the prior remains fairly broad ($\text{Var}[\text{Beta}(3, 2)] = 0.04$), letting the data dominate whenever there are enough counts. After sampling in the unbounded logit variable u , the Jacobian $\ln[f(1 - f)]$ is used to correctly map back to a Beta(α, β) prior on f_{RC} .

Posterior Sampling—The posterior

$$\ln p(\vec{\theta} | \text{data}) = \ln \mathcal{L} + \ln p(\vec{\theta})$$

is mapped with an affine-invariant `EnsembleSampler` from `emcee` (Foreman-Mackey et al. 2013). The sampler is set for 64 walkers, 15000 steps, with a 1000 step burn-in. These values are justified from the autocorrelation analysis described in Section 3.3. For every tile

$$\langle \mu \rangle, \langle \sigma \rangle, \langle A \rangle, \langle f_{\text{RC}} \rangle,$$

are stored as the posterior medians, and the posterior standard deviation of μ ,

$$\sigma_\mu = \sqrt{\text{Var}_{\text{post}}(\mu)},$$

serves as the uncertainty on the RC centroid (still in the rotated basis).

Back-rotation—The representative CMD position (original basis) of the tile is

$$\vec{r}_{\text{CMD}} = \hat{R}^T \begin{pmatrix} \langle x_{\text{rot}} \rangle \\ \langle \mu \rangle \end{pmatrix}$$

where $\langle x_{\text{rot}} \rangle$ is the median x_{rot} of all the stars in the tile. Uncertainty propagation (back to the original basis) uses

$$\vec{\sigma}_{\text{CMD}} = \hat{R}^T \begin{pmatrix} 0 \\ \sigma_\mu \end{pmatrix}, \quad \sigma_y = |(\vec{\sigma}_{\text{CMD}})_2|.$$

Only tiles with

$$\sigma_y \leq 0.3 \text{ mag}, \quad \text{and} \quad f_{\text{RC}} > 0.01 \quad (4)$$

(i.e. have an RC population), and have satisfied autocorrelation as described in Section 3.3 are retained for the final linear regression.

Weighted linear regression—The total RC area inside each tile is

$$A_i = A_i \sigma_i \sqrt{2\pi}, \quad A_i^{(\text{norm})} = \frac{A_i}{\max_j A_j} \in (0, 1].$$

Adopting the inverse-variance logic of χ^2 fitting, but down-weighting tiles where the RC population is intrinsically faint or poorly populated (smaller f_{RC}), the weights

$$w_i = A_i^{(\text{norm})} \frac{f_{\text{RC}, i}}{\sigma_{y,i}^2}.$$

are assigned. In other words, tiles with more RC stars count more. Finally, a weighted linear regression through the representative points from all tiles $(x_i, y_i) = (\vec{r}_{\text{CMD}})^T$ yields

$$y = \hat{m}x + \hat{b}, \quad \text{Cov}(\hat{m}, \hat{b}) = C, \quad \sigma_{\hat{m}} = \sqrt{C_{00}}.$$

The pair $(\hat{m} \pm \sigma_{\hat{m}})$ constitutes the final extinction ratio. This procedure is performed for all three CMDs in all four NRCB footprints. Method 2 is outlined in the appendix as it is only a verification for Method 1’s measurements on F115W-F323N vs. F115W CMDs.

3.3. Autocorrelation Analysis

`emcee`’s `EnsembleSampler` (Foreman-Mackey et al. 2013) yields *correlated* draws, where samples from walks are not statistically independent. A way of quantifying that correlation is via the **integrated autocorrelation time**

$$\tau_{\text{int}}(m) = 1 + 2 \sum_{s=1}^{\infty} \rho_m(s), \quad \rho_m(s) = \frac{\text{Cov}(\theta_m^{(t)}, \theta_m^{(t+s)})}{\text{Var}(\theta_m)},$$

computed for each parameter θ_m . Intuitively, τ_{int} measures over how many steps the chain “forgets” its past; the effective number of independent draws in a run of length N is N/τ_{int} .

While it is not formally possible to guarantee convergence for a nontrivial MCMC, experience with ensemble samplers like emcee shows that a walker whose length satisfies

$$N \gtrsim 50 \tau_{\text{int}}$$

is typically long enough for a reliable estimation of means and 1σ credible intervals.

$$\hat{\tau}_{\text{int}}(N) = \text{mean over parameters}[\tau_{\text{int}, m}(N)]$$

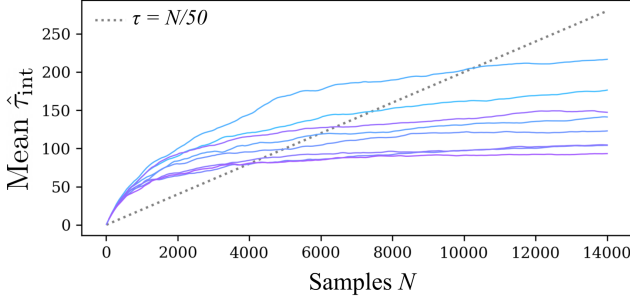


Figure 5. Integrated autocorrelation time $\hat{\tau}_{\text{int}}$ as a function of total samples N for 8/10 CMD tiles from NRCB1 F115W - F212N vs. F115W that satisfied Equation 4. Each colored curve tracks the mean autocorrelation across all sampled parameters in one tile. The black dashed line denotes the heuristic convergence criterion $\tau = N/50$. Curves that flatten below the dashed line by $N \approx 10^4$ indicate that the 15000 step runs achieve an effective number of independent samples sufficient for reliable posterior estimation.

is monitored as the MCMC run(s) from Sections 3.2.1 and A progress. The final chain length(s) N is adjusted to exceed $50 \tau_{\text{int}}$. Figure 5 plots $\hat{\tau}_{\text{int}}$ against the number of samples N for the 8/10 CMD tiles from NRCB1 F115W - F212N vs. F115W whose σ_y and f_{RC} satisfied the criterion in Section 3.2.1.0.

However, in the Method 1 CMD procedure (Section 3.2.1), some bins never satisfy $\hat{\tau}_{\text{int}} < N/50$ even for very long chains, because they contain too few stars. To ensure both per-tile convergence and a robust set of points for the final fit,

1. The number of tiles is fixed to $n = 10$.
2. Any tile whose sampler still fails $\tau_{\text{int}} \lesssim N/50$ after the run is discarded.

This guarantees that every remaining bin meets the autocorrelation criterion while providing enough (x_k, μ_k) pairs for global linear regression. For the Method 2 CMD procedure (Section A), the chain length N is just chosen large enough to satisfy autocorrelation, as linear regression is performed on the full RC cluster rather than individual tiles.

4. RESULTS

Tables 2 and 3 summarize our results. Figure 7 displays our extinction ratios relative to other GC extinction laws. At F115W the total-to-selective ratios span 3.25 to 3.65, drop to unity at F212N, and stabilize at 0.58 to 0.67 (F323N) and 0.395 to 0.429 (F405N). Av-

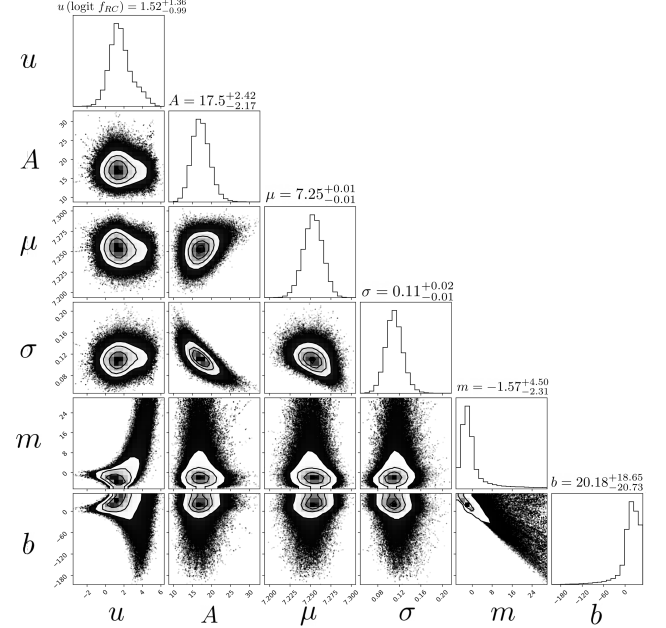


Figure 6. Corner plot of the MCMC posterior for NRCB1 F115W-F212N versus F115W (tile $k = 3$).

eraged over all NRCB fields, the extinction ratios are

$$\frac{A_{\text{F115W}}}{A_{\text{F212N}}} = 3.46 \pm 0.06, \quad \frac{A_{\text{F323N}}}{A_{\text{F212N}}} = 0.63 \pm 0.08 \\ \frac{A_{\text{F405N}}}{A_{\text{F212N}}} = 0.38 \pm 0.02,$$

and $A_{\text{F212N}}/A_{\text{F212N}} = 1$. Spatial variation appears only in the short wavelength ratio $A_{\text{F115W}}/A_{\text{F212N}}$; the longer wavelength ratios remain uniform across all fields (Section 4.1). Formal uncertainties are $\approx 2\%$ at F115W, $\approx 13\%$ at F323N, and $\approx 5\%$ at F405N, corresponding to signal-to-noise ratios of roughly 60, 8, and 19, respectively.

4.1. Spatial Homogeneity

The extinction ratios were cross-compared among the four detectors to test for spatial variation. At $1.15\mu\text{m}$ the only $> 3\sigma$ discrepancy is between NRCB3 and NRCB4 ($|z| = 3.2$, $p = 1.4 \times 10^{-3}$). NRCB2 shows a moderate offset from NRCB3 ($|z| = 2.6$, $p = 8.8 \times 10^{-3}$) but is technically consistent with NRCB1 and NRCB4 ($|z| \leq 1.6$, $p \geq 0.06$). NRCB1 and NRCB3 are statistically identical $|z| = 0.05$, $p = 0.96$ (see Figure 10). No spatial variation is detected at F323N or F405N ($p > 0.5$); a single curve suffices at $3 - 4\mu\text{m}$. Hence, extinction toward the GC is slightly grayer in NRCB2 and NRCB4 at $\sim 1.15\mu\text{m}$ but otherwise uniform across the inner $120'' \times 120''$.

Table 2. Measured slopes of the RC bar: total-to-selective ratios $A_{F115W}/E(F115W - \lambda)$ for each NRCB field, their means across all four footprints, and the predicted slopes using the Fritz et al. (2011) law.

λ	NRCB1	NRCB2	NRCB3	NRCB4	Mean	Fritz et al. (2011)
F212N	1.3784 ± 0.0289	1.4336 ± 0.0147	1.3767 ± 0.0153	1.4453 ± 0.0139	1.4085 ± 0.0182	1.3963
F323N	1.1893 ± 0.1132	1.2522 ± 0.0503	1.2060 ± 0.0237	1.2460 ± 0.0485	1.2182 ± 0.0572	1.2228
F405N	1.1256 ± 0.0211	1.1335 ± 0.0225	1.1168 ± 0.0103	1.1233 ± 0.0090	1.1361 ± 0.0139	1.1194

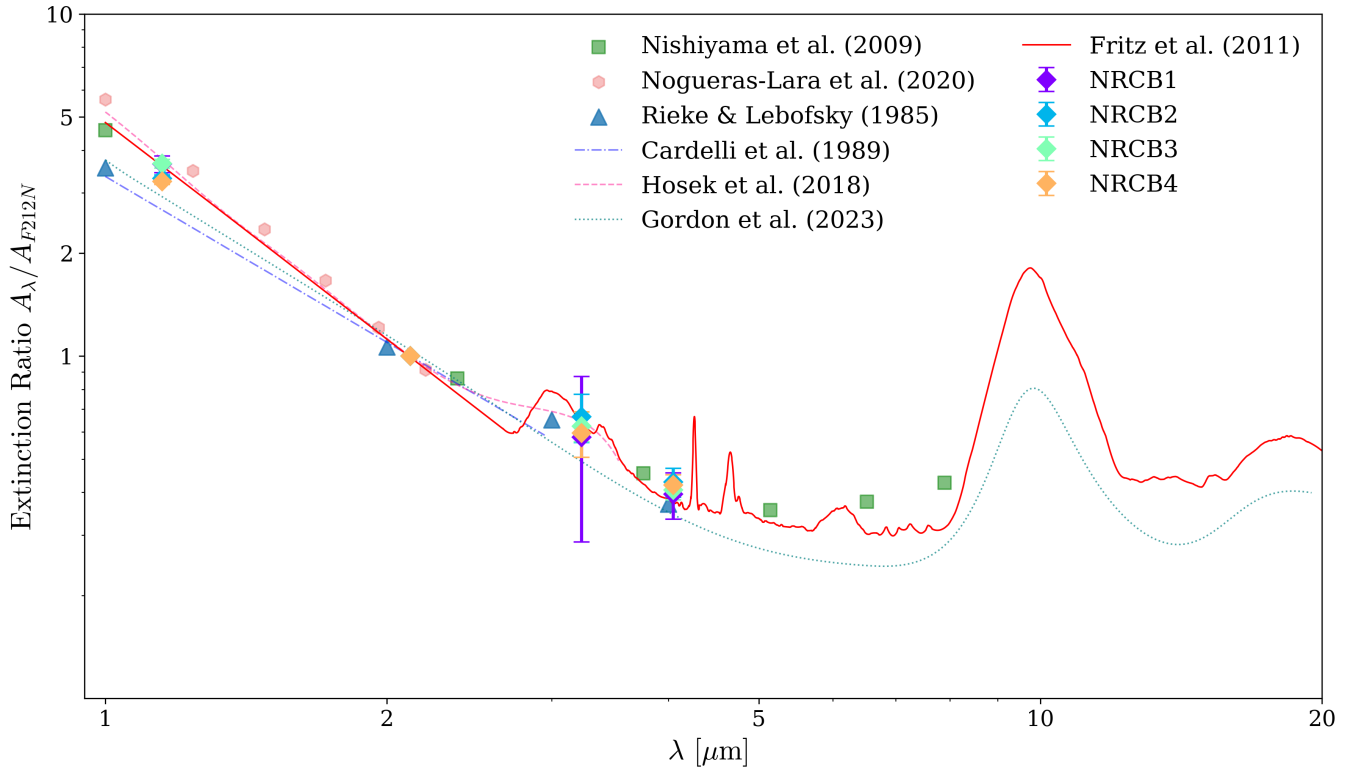


Figure 7. Discrete near-infrared extinction measurements for all NRCB $60'' \times 60''$ footprints in the Galactic Center. The red solid curve shows the Fritz et al. (2011) GC extinction law (NRCB3), the dashed pink line shows the Hosek et al. (2018) GC extinction law, green squares mark the Nishiyama et al. (2009) law, blue triangles denote the Rieke & Lebofsky (1985) law, and pink hexagons show the Nogueras-Lara et al. (2020) law. The dashed blue and dotted teal lines indicate the diffuse Milky Way ISM laws of Cardelli et al. (1989) and Gordon et al. (2023), respectively. Laws were rendered using SPISEA (Hosek et al. 2020).

4.2. Extinction Law Versus Total Extinction

This test determines whether the distinct extinction curves seen in the four NRCB footprints reflect differences in their mean dust columns/total extinction. For each RC star, the quantities

$$x \equiv m_{F212N}, \quad y_\lambda \equiv \frac{m_\lambda - m_{F212N}}{m_{F115W} - m_{F212N}},$$

with $\lambda \in \{F323N, F405N\}$ were plotted. Apparent magnitudes satisfy $m_\nu = M_\nu + \mu + A_\nu$; with the near-constant RC absolute magnitude M_{F212N} , x acts

as a proxy for the total extinction A_{F212N} . Let $R_\lambda \equiv A_\lambda / A_{F212N}$ and $R_{F115W} \equiv A_{F115W} / A_{F212N}$, and define the (small) intrinsic RC colors $C_{0,\lambda} = M_\lambda - M_{F212N}$ and $C_{0,F115W} = M_{F115W} - M_{F212N}$. Then

$$y_\lambda = \frac{C_{0,\lambda} + (R_\lambda - 1)A_{F212N}}{C_{0,F115W} + (R_{F115W} - 1)A_{F212N}}.$$

Since $C_{0,\lambda}$, $C_{0,F115W} \lesssim 0.02$ mag and $A_{F212N} \gtrsim 1$ mag, the color terms are negligible, giving

$$y_\lambda \simeq \frac{R_\lambda - 1}{R_{F115W} - 1} \Rightarrow R_\lambda = 1 + (R_{F115W} - 1)y_\lambda.$$

Table 3. Final extinction ratios A_λ/A_{F212N} for NRCB1–4, their mean, and comparisons to other GC extinction laws.

A_λ/A_{F212N}	This study					Literature ^a				
	NRCB1	NRCB2	NRCB3	NRCB4	Mean	F11 ^b	N09	NL20	HK18	HG24
$\simeq 1.15\mu\text{m}$	3.64 ± 0.20	3.31 ± 0.08	3.65 ± 0.11	3.25 ± 0.07	3.46 ± 0.06	3.63 ± 0.16	3.42	4.12	3.76	—
$\simeq 1.65\mu\text{m}^c$	1.63 ± 0.10	1.48 ± 0.05	1.64 ± 0.07	1.46 ± 0.05	1.55 ± 0.04	1.63 ± 0.08	1.65	1.84	1.71	1.67 ± 0.05
$\simeq 3.23\mu\text{m}$	0.58 ± 0.29	0.67 ± 0.11	0.62 ± 0.06	0.64 ± 0.10	0.63 ± 0.08	0.64 ± 0.06	0.56	—	0.64	—
$\simeq 3.80\mu\text{m}^d$	0.47 ± 0.24	0.54 ± 0.09	0.50 ± 0.06	0.52 ± 0.09	0.50 ± 0.07	0.41 ± 0.05	0.45	—	—	0.69 ± 0.03
$\simeq 4.05\mu\text{m}$	0.41 ± 0.06	0.39 ± 0.06	0.38 ± 0.03	0.36 ± 0.02	0.38 ± 0.02	0.37 ± 0.05	0.42	—	—	—

^aF11: Fritz et al. (2011); N09: Nishiyama et al. (2009); NL20: Nogueras-Lara et al. (2020); HK18: Hosek et al. (2018, 2020); HG24: Haggard et al. (2024).

^bUncertainties are from the nearest Fritz wavelength measurement to λ (maximum $\Delta\lambda = 0.01\mu\text{m}$).

^cRatios extrapolated using power-law index $\alpha = 2.30 \pm 0.08$ from Nogueras-Lara et al. (2018).

^dRatios extrapolated using power-law index $\alpha = 1.34 \pm 0.29$ from Schödel et al. (2010).

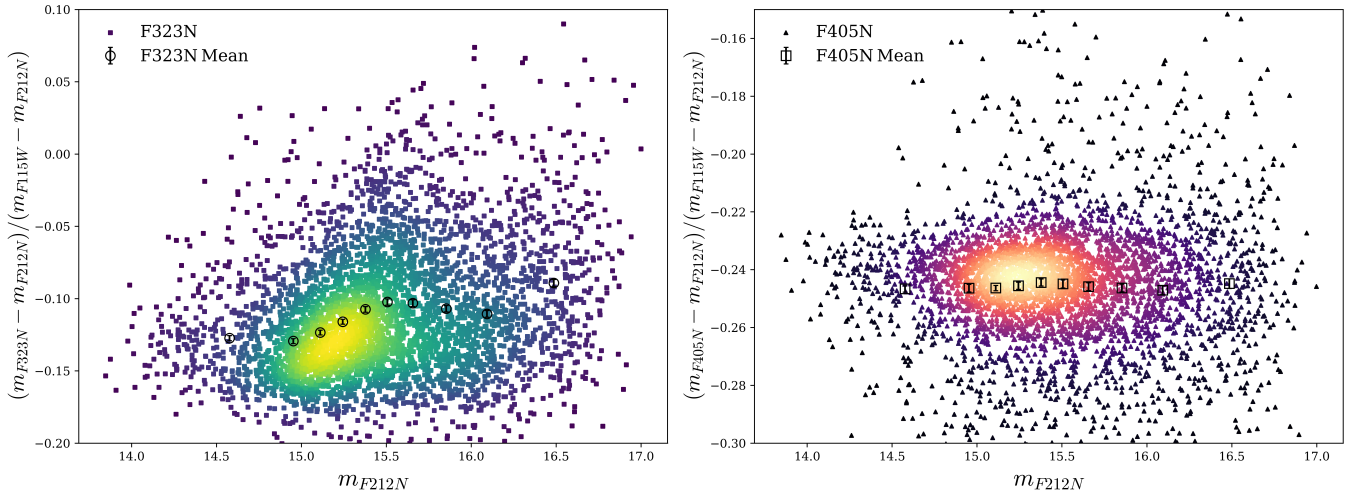


Figure 8. Extinction ratio vs. Total Extinction proxy for NRCB1. RC stars are plotted as F323N circles and F405N triangles. The horizontal axis m_{F212N} traces total extinction A_{F212N} , while the vertical axis $y_\lambda = (m_\lambda - m_{F212N})/(m_{F115W} - m_{F212N})$ encodes A_λ/A_{F212N} . The near-horizontal trends in all NRCB footprints show that the extinction ratios at $3.23\mu\text{m}$ and $4.05\mu\text{m}$ are roughly independent of column density.

A horizontal y_λ - x trend therefore indicates that R_λ (and thus the NIR extinction law) is independent of the local NRCB dust column, while any slope signals a systematic link between the shape of the extinction curve and the total extinction within the footprint.

Across all four NRCB footprints the y_λ - m_{F212N} planes are flat for $\lambda = \text{F405N}$, indicating that $A_{\text{F405N}}/A_{\text{F212N}}$ is independent of total extinction A_{F212N} (Figure 8). The F323N ridge shows a shallow positive slope (0.016–0.024), but Monte Carlo resampling that propagates photometric catalog errors in

m_{F115W} , m_{F212N} , and m_{F323N} yields two-tailed probabilities $p \simeq 0.35$ of obtaining such slopes by chance in every footprint. The ratio $A_{\text{F323N}}/A_{\text{F212N}}$ is therefore also consistent with being constant over the full range of A_{F212N} .

5. DISCUSSION

The discrete extinction measurements span only three NIR bands (plus the 1.0 anchor at F212N), yet they reveal clear spatial variations at short wavelengths. The wavelength dependence of extinction is governed by the

Mie size parameter, $x = 2\pi a/\lambda$ (Bohren & Huffman 1983). In the near-infrared Rayleigh regime ($x \ll 1$), $A_\lambda \propto \lambda^{-1}$, while for $x \gtrsim 1$ the extinction becomes effectively gray (Draine 2011). Defining the transition radius

$$a_{\text{trans}} = \frac{\lambda}{2\pi} \approx 0.18 \left(\frac{\lambda}{1.15 \mu\text{m}} \right) \mu\text{m},$$

a flatter extinction at $1.15 \mu\text{m}$ in NRCB2 and NRCB4 implies a size distribution skewed toward grains with $a \gtrsim 0.1 - 0.2 \mu\text{m}$ (or equivalently, a depletion of $a \lesssim 0.1 \mu\text{m}$) that suppress the Rayleigh λ^{-1} slope (Mathis et al. 1977; Weingartner & Draine 2001). At $3 - 4 \mu\text{m}$, every grain satisfies $x \ll 1$ explaining the uniform agreement with the Fritz et al. (2011) curve at F323N and F405N. However, because NRCB1 and NRCB3 do not exhibit flattened extinction at $\sim 1.15 \mu\text{m}$, any global GC extinction law must include spatially dependent corrections when high precision is required.

5.1. Comparison to Fritz et al. (2011)

Crucially, the extinction ratios for NRCB3, which contains the $14'' \times 20''$ region around Sgr A^* used by Fritz et al. (2011), are in agreement with their results. The NRCB3 measurements deliver uncertainties that are roughly 30% tighter at F115W ($\sim 1.15 \mu\text{m}$), 0% tighter at F323N ($\sim 3.23 \mu\text{m}$), and 40% tighter at F405N ($\sim 4.05 \mu\text{m}$). When averaged across the four NRCB footprints, the uncertainties improve by $\approx 63\%$ at F115W and $\approx 60\%$ at F405N (with somewhat larger scatter at F323N driven by field-to-field variation, with a $\approx 380\%$ wider uncertainty in NRCB1).

5.2. Comparison to other GC Laws

Table 3 lists the present ratios A_λ/A_{F212N} alongside the Fritz et al. (2011) measurements, and Nishiyama et al. (2009) (N09), Nogueras-Lara et al. (2020) (NL20), Hosek et al. (2018, 2020) (HK18). The measured extinction ratios using high-proper-motion stars from Haggard et al. (2024) (HG24) are also shown at H ($1.63 \mu\text{m}$) and L' ($3.80 \mu\text{m}$).

$1.15 \mu\text{m}$.— The footprint-averaged ratio

$$\left\langle \frac{A_{F115W}}{A_{F212N}} \right\rangle = 3.46 \pm 0.06$$

lies between H18 (3.76) and N09 (3.42) and is 11σ below NL20 (4.13). NRCB2 and NRCB4 give 3.31 ± 0.08 and 3.25 ± 0.07 , differing from all laws by $10 - 13\sigma$; NRCB1 and NRCB3 agree with N09 and H18 within $1 - 2\sigma$.

Extrapolation to the H band.— Using the NIR power-law index $\beta = 2.30 \pm 0.08$ from Nogueras-Lara et al.

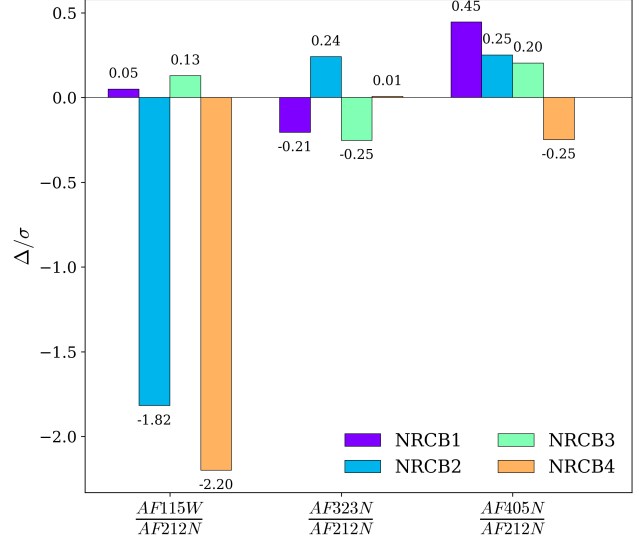


Figure 9. Total extinction A_λ significance relative to Fritz et al. (2011) across all NRCB footprints.

(2018), $A_H/A_{F212N} = (A_{F115W}/A_{F212N})(1.63/1.15)^{-\beta}$ yields $A_H/A_{F212N} = 1.63 \pm 0.10$ (NRCB1), 1.48 ± 0.05 (NRCB2), 1.64 ± 0.07 (NRCB3), and 1.46 ± 0.05 (NRCB4). HG24 report $A_H/A_{K'} = 1.67 \pm 0.05$, consistent with NRCB1 and NRCB3 but higher than NRCB2 and NRCB4 by roughly 3σ . These NRCB ratios are extrapolated though, not directly measured, so any offset from HG24 may stem from the assumed power law.

$3.23 \mu\text{m}$.— All footprints cluster at $A_{F323N}/A_{F212N} = 0.63 \pm 0.08$, matching H18 (0.64) within 1σ and N09 (0.56) within 1σ .

Extrapolation to $3.8 \mu\text{m}$.— Applying Schödel et al. (2010)'s mid-IR index $\beta = 1.34 \pm 0.29$ to the mean F323N ratio gives $A_{3.8}/A_{F212N} = 0.50 \pm 0.07$. By contrast, HG24 report $A_{L'}/A_{K'} = 0.69 \pm 0.03$, larger by 2.5σ . H24 suggests this large discrepancy may be from their proper-motion stars tracing locally altered grain populations in the central parsec, which drive steeper grain tracks in NIR color-color space. In our $\sim 5.4 \text{pc}^2$ JWST footprints we see no evidence for a steeper $A_{3.80 \mu\text{m}}$, suggesting there are *even smaller* variations of extinction within the central GC.

$4.05 \mu\text{m}$.— The uniform ratio $A_{F405N}/A_{F212N} = 0.38 \pm 0.02$ agrees with N09 (0.417) within the stated uncertainties.

Interestingly, Nogueras-Lara et al. (2020) (NL20) concludes that there is no significant variation of the extinction curve with wavelength with the line-of-sight. NL20 analyzed a high angular resolution ($\sim 0.2''$) JHK_s survey covering $\sim 6000 \text{pc}^2$ and fitted a synthetic Kurucz red-clump (RC) model (Nogueras-Lara et al. 2018)

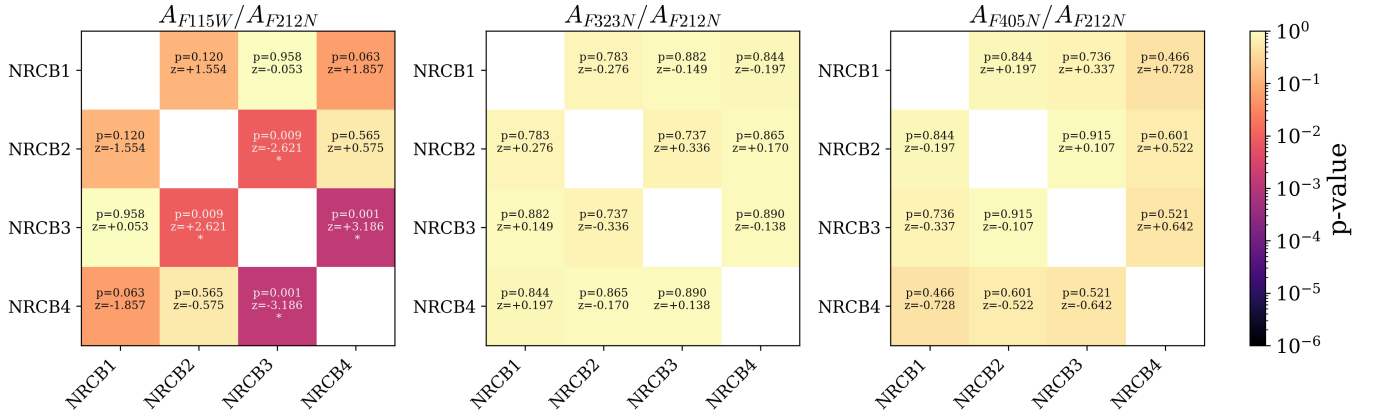


Figure 10. Heatmaps of pairwise p -values (log scale) and Z -scores comparing extinction ratios A_λ/A_{F212N} across NRCB1–4. Asterisks mark $p < 0.05$; darker cells indicate higher significance.

through a fine grid in power-law index (β) and absolute extinction ($A_{1.61}$). The combination of a broad J band ($\lambda \simeq 1.25 \mu\text{m}$) with model-based fitting and a $\sim 0.2''$ PSF, which blurs structure on scales $\lesssim 0.008 \text{ pc}$ at 8 kpc, led NL20 to conclude that the extinction curve does not show significant variation with the line-of-sight

However, JWST NIRCam’s short wavelength channel samples the sky at $0.031''/\text{pixel}$ and is diffraction limited to a PSF of $\simeq 0.04''$ at $1.15 \mu\text{m}$ rising to $\simeq 0.06''$ at $2.12 \mu\text{m}$, corresponding to physical scales of ~ 0.001 – 0.002 pc at 8 kpc. We also measure the RC ridge slopes directly at ($\lambda = 1.15 \mu\text{m}$). This reveals a $\sim 10\%$ graying in NRCB2 and NRCB4, equivalent to a ~ 2 – 3σ variation in A_{F115W}/A_{F212N} . The longer wavelength ratios F323N, F405N remain spatially uniform.

Thus, the extinction curve is uniform across the $\sim 6000 \text{ pc}^2$ area surveyed by NL20 at an angular resolution of $\sim 0.2''$, but shows short wavelength differences between the analyzed JWST footprints.

6. CONCLUSION

We have derived near-infrared extinction ratios A_λ/A_{F212N} in four regions covering the central $120'' \times 120''$ of the Galactic Center using 21,195 red clump stars observed by JWST. Linear regressions of the RC ridges in three color–magnitude diagrams across all regions yield mean absolute extinction ratios

$$\begin{aligned} \frac{A_{F115W}}{A_{F212N}} : \frac{A_{F212N}}{A_{F212N}} : \frac{A_{F323N}}{A_{F212N}} : \frac{A_{F405N}}{A_{F212N}} \\ 3.46 \pm 0.06 : 1.00 : 0.62 \pm 0.08 : 0.41 \pm 0.02 \end{aligned}$$

The methods used rely only on RC geometry, free of any stellar evolution models, but assumes all RC color spread arises from interstellar extinction.

At $1.15 \mu\text{m}$ the ratio A_{F115W}/A_{F212N} differs between the four regions: NRCB2 (3.31 ± 0.08) and NRCB4 (3.25 ± 0.07) are flatter than NRCB1 and NRCB3 by 2 – 3σ and flatter than the Fritz et al. (2011) curve by 1 – 2σ

(Figure 9). This localized graying implies a grain-size distribution biased toward radii $a \gtrsim 0.1$ – $0.2 \mu\text{m}$ in these regions (Section 5). In contrast, the $3.23 \mu\text{m}$ and $4.05 \mu\text{m}$ ratios are statistically indistinguishable across all fields, confirming that once the Rayleigh regime is reached ($\lambda \gtrsim 3 \mu\text{m}$) the extinction curve is spatially uniform.

An independent test compares the extinction ratios with the total dust column within each region. For both F323N and F405N, fits of normalized color $y_\lambda \equiv (m_\lambda - m_{F212N})/(m_{F115W} - m_{F212N})$ against m_{F212N} yield slopes consistent with zero within Monte Carlo uncertainties (two-tailed $p \simeq 0.35$). We therefore conclude that the shape of the extinction law is independent of column density across the sampled range; the variations seen at $1.15 \mu\text{m}$ reflect intrinsic grain size differences rather than differences in total dust.

The NRCB3 region, containing $14'' \times 20''$ patch around Sgr. A* analyzed by Fritz et al. (2011), reproduces their extinction law at all measured wavelengths within 1σ , validating both approaches. Departures appear only in adjacent regions and only at $1.15 \mu\text{m}$, showing that systematic differences originate in the transition from Rayleigh to Mie regimes rather than in the long wavelength tail. The associated uncertainties in NRCB3 improve on those of Fritz et al. (2011) by roughly 30 % at $1.15 \mu\text{m}$, 0 % at $3.23 \mu\text{m}$, and 40 % at $4.05 \mu\text{m}$.

These results demonstrate that a single extinction curve cannot describe the GC at $\lambda \lesssim 2.12 \mu\text{m}$ even on sub-parsec scales, whereas the long-wavelength ratios remain constant. Any precision photometry or stellar population analysis in the central GC must therefore apply location-specific corrections at short wavelengths while safely adopting a common curve beyond $3 \mu\text{m}$.

Together, these measurements refine the average GC extinction law and reveal significant spatial variations in dust properties on scales below one parsec – an effect

that must be accounted for in precision studies of the Galactic Center.

REFERENCES

- Benjamin, R. A., Churchwell, E., Babler, B. L., et al. 2003, *PASP*, 115, 953
- Bohren, C. F., & Huffman, D. R. 1983, *Absorption and Scattering of Light by Small Particles* (New York: Wiley-Interscience)
- Boogert, A. C. A., Gerakines, P. A., & Whittet, D. C. B. 2015, *ARA&A*, 53, 541
- Cardelli, J. A., Clayton, G. C., & Mathis, J. S. 1989, *ApJ*, 345, 245
- De Marchi, G., Panagia, N., Sabbi, E., et al. 2016, *MNRAS*, 455, 4373
- Draine, B. T. 1989, in ESA SP-290, *Infrared Spectroscopy in Astronomy*, ed. B. H. Kaldeich (Noordwijk: ESA), 93
- Draine, B. T. 2003, *ARA&A*, 41, 241
- Draine, B. T. 2011, *Physics of the Interstellar and Intergalactic Medium* (Princeton, NJ: Princeton Univ. Press)
- Fahrion, K., Seth, A. C., Bastian, N., et al. 2023, *A&A*, 671, L14
- Fitzpatrick, E. L. 1999, *PASP*, 111, 63
- Fitzpatrick, E. L., & Massa, D. 2007, *ApJ*, 663, 320
- Fitzpatrick, E. L., & Massa, D. 2009, *ApJ*, 699, 1209
- Foreman-Mackey, D., Hogg, D. W., Lang, D., & Goodman, J. 2013, *PASP*, 125, 306
- Freedman, W. L., Madore, B. F., Gibson, B. K., et al. 2001, *ApJ*, 553, 47
- Fritz, T. K., Gillessen, S., Dodds-Eden, K., et al. 2011, *ApJ*, 737, 73
- Froebrich, D., Murphy, G. C., Smith, M. D., et al. 2007, *MNRAS*, 378, 1447
- Gao, J., Jiang, B. W., & Li, A. 2009, *ApJ*, 707, 89
- Gao, J., Jiang, B. W., & Li, A. 2013, *ApJ*, 776, 7
- Girardi, L., Bressan, A., Bertelli, G., & Chiosi, C. 2001, *A&AS*, 141, 371
- Girardi, L. 2016, *ARA&A*, 54, 95
- Ginsburg, A., Barnes, A. T., Battersby, C. D., et al. 2023, *ApJ*, 959, 36
- Goodman, J., & Weare, J. 2010, *Commun. Appl. Math. Comput. Sci.*, 5, 65
- Gordon, K. D., Clayton, G. C., Decleir, M., et al. 2023, *ApJ*, 950, 86
- Green, G. M., Schlafly, E. F., Finkbeiner, D. P., et al. 2015, *ApJ*, 810, 25
- Haggard, Z., Ghez, A. M., Sakai, S., et al. 2024, *AJ*, 168, 166
- Hosek, M. W., Jr., Lu, J. R., Anderson, J., et al. 2018, *ApJ*, 855, 13
- Hosek, M. W., Jr., Lu, J. R., Anderson, J., et al. 2019, *ApJ*, 870, 44
- Hosek, M. W., Jr., Lu, J. R., Lam, C. Y., et al. 2020, *AJ*, 160, 143
- Khan, S., Anderson, R. I., Miglio, A., Mosser, B., & Elsworth, Y. P. 2023, *A&A*, 680, A105
- Lada, C. J., & Lada, E. A. 2003, *ARA&A*, 41, 57
- Li, A., Chu, Y.-H., Stahl, O., et al. 2024, *ApJL*, 968, L26
- Martin, P. G., & Whittet, D. C. B. 1990, *ApJ*, 357, 113
- Mathis, J. S., Rumpl, W., & Nordsieck, K. H. 1977, *ApJ*, 217, 425
- Messineo, M., Habing, H. J., Menten, K. M., et al. 2005, *A&A*, 435, 575
- Minniti, D., Lucas, P. W., Emerson, J. P., et al. 2010, *New Astron.*, 15, 433
- Nishiyama, S., Tamura, M., Hatano, H., et al. 2009, *ApJ*, 696, 1407
- Nogueras-Lara, F., Gallego-Calvente, A. T., Dong, H., et al. 2018, *A&A*, 610, A83
- Nogueras-Lara, F., Schödel, R., Gallego-Calvente, A. T., et al. 2019, *A&A*, 631, A20
- Nogueras-Lara, F., Schödel, R., Neumayer, N., et al. 2020, *A&A*, 641, A141
- Nogueras-Lara, F., Schödel, R., Dong, H., et al. 2021, *A&A*, 654, A81
- Rieke, G. H., & Lebofsky, M. J. 1985, *ApJ*, 288, 618
- Schlafly, E. F., Schlegel, D. J., Green, G. M., et al. 2016, *ApJ*, 821, 78
- Schödel, R., Najarro, F., Muzic, K., & Eckart, A. 2010, *A&A*, 511, A18
- Schödel, R., Nogueras-Lara, F., Mauerhan, J., et al. 2025, arXiv:2310.11912
- Schlutheis, M., Robin, A. C., Reylé, C., et al. 2009, *A&A*, 495, 157
- Voshchinnikov, N. V., Il'in, V. B., Henning, T., & Akhtemov, Z. S. 2017, *A&A*, 605, A40
- Wang, T., Calzetti, D., Whitmore, B. C., et al. 2024, *ApJL*, 964, L3
- Weingartner, J. C., & Draine, B. T. 2001, *ApJ*, 548, 296
- Wozniak, P. R., & Stanek, K. Z. 1996, *ApJ*, 464, 233

APPENDIX

A. METHOD 2

A second approach for estimating the total-to-selective extinction ratio is applied to CMDs in which the Red Clump (RC) ridge is broader or less sharply defined. This method serves to cross-validate the RC ridge slopes calculated with Method 1 (Section 3.2.1). Both approaches are designed to minimize subjective choices in the analysis (i.e., where to cutoff the RC relative to the surrounding CMD and how to set the initial parameter guesses for the MCMC) by using automated procedures to isolate and characterize the RC as fully as possible.

Input: RC region, gap g , top fraction f_{top}

Input: trials N , jitter amplitude ϵ

Output: $m \pm \hat{\sigma}_m$

Pick two guide points and choose gap g .

Compute anchor line (m_0, b_0) through guide points.

$S \leftarrow \{k : |\mu_k - (m_0 x_k + b_0)| \leq g\} // \pm g/2 \text{ color band}$
 $S \leftarrow \text{densest } f_{\text{top}} \text{ of } S \text{ via KDE.} // \text{ focus on RC}$

$(m, \sigma_{\text{stat}}) \leftarrow \text{MCMC_LINEAR}(S)$

for $t = 1$ **to** N **do**

$\tilde{S}_t \leftarrow \text{jitter inputs/anchors by } \pm \epsilon;$
 $m_t \leftarrow \text{Slope}(\text{MCMC_LINEAR}(\tilde{S}_t));$

end

$\sigma_{\text{sys}} \leftarrow \text{StdDev}(\{m_t\}_{t=1}^N)$

$\hat{\sigma}_m = \sqrt{\sigma_{\text{stat}}^2 + \sigma_{\text{sys}}^2}$.

return $m \pm \hat{\sigma}_m$

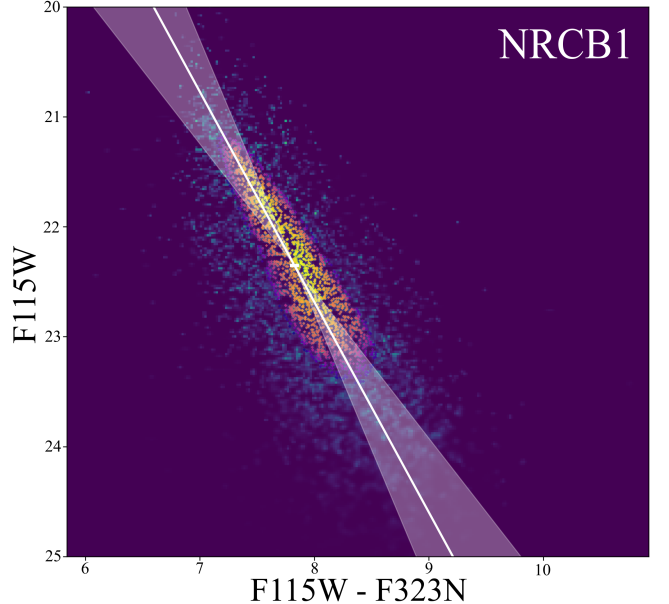


Figure 11. *Left:* Overview of the algorithm used to measure the RC ridge slope in CMDs where the RC is broad or poorly defined. *Right:* Application of Method 2 to the F115W-F323N versus F115W CMD in NRCB1. The $f_{\text{top}} = 0.4$ highest-density stars are overplotted on the unsharp masked Hess diagram; the white line shows the best fit linear slope from the MCMC posterior, and the shaded band shows the uncertainty envelope obtained from $N = 500 \pm \epsilon \sim 30\%$ jitter Monte Carlo MCMC sweeps. This cross-check is used only for the F115W–F323N versus F115W CMDs for all NRCB footprints.

For F115W - F323N vs. F115W CMDs, the color is defined as $x = m_{F115W} - m_{F323N}$ and magnitude $y = m_{F115W}$ with photometric error σ_y . Two bye-eye points $(x_1, y_1), (x_2, y_2)$ with a half-width gap g specify an initial strip

$$\mathcal{B}_0 = \{(x, y) : |y - (m_0 x + b_0)| \leq g\},$$

where m_0 is the slope of the anchor line between the points $(x_1, y_1), (x_2, y_2)$ and b_0 is its intercept. To avoid diluting the fit with sparse outskirts, only the densest f_{top} of points within \mathcal{B}_0 are retained. Density is estimated via a 2D kernel density estimator (KDE): $\rho(x, y) = \hat{p}_{\text{KDE}}(x, y)$. Stars whose ρ exceeds the $(1 - f_{\text{top}})$ -quantile of the KDE distribution are kept. In practice $f_{\text{top}} \simeq 0.4$ to give an ample number of stars for a robust fit while focusing on the RC. This process is visualized on the right of Figure 11.

Bayesian model—Let the final filtered set contain N stars. The data-generating equation is posited.

$$y_i = mx_i + b + \varepsilon_i, \quad \varepsilon_i \sim \mathcal{N}(0, \sigma_y^2(x_i) + \sigma_{\text{int}}^2),$$

where (m, b) are the RC slope and intercept, $\sigma_y(x_i)$ is the known photometric error, and σ_{int} is any other error besides measurement. Sampling in logarithmic space, $\log \sigma_{\text{int}} \equiv \eta$, keeps the parameter unbounded. The log-likelihood is

$$\ln \mathcal{L}(m, b, \eta) = -\frac{1}{2} \sum_{i=1}^N \left[\frac{(y_i - (mx_i + b))^2}{\sigma_y^2(x_i) + e^{2\eta}} + \ln(2\pi [\sigma_y^2(x_i) + e^{2\eta}]) \right].$$

Table 4. F115W–F323N vs. F115W RC ridge slope measurements using Method 1 (3.2.1) and Method 2 (A). Only Method 1’s measurements were used in the extinction ratio analysis.

Method	NRCB1	NRCB2	NRCB3	NRCB4	Mean
1	1.1893 ± 0.1132	1.2522 ± 0.0503	1.2060 ± 0.0237	1.2460 ± 0.0485	1.2187 ± 0.0193
2	1.2056 ± 0.1157	1.2428 ± 0.1452	1.2258 ± 0.1648	1.2897 ± 0.1521	1.2410 ± 0.0728
Δ/σ	0.10	-0.06	0.12	0.27	0.30

Broad priors are adopted

$$m \sim \text{Uniform}(-10^3, 10^3), \quad b \sim \text{Uniform}(-10^6, 10^6), \quad p(\eta) \propto \exp\left(-\frac{1}{2}\eta^2\right).$$

The posterior is explored with 40 affine-invariant walkers for 6000 steps with a 1000 step burn-in. Let the posterior medians be $\hat{m}, \hat{b}, \hat{\sigma}_{\text{int}}$ and the statistical 1σ error, $\sigma_{\hat{m}, \text{stat}} = \sqrt{\text{Var}_{\text{post}}(m)}$. To gauge how much the result depends on the initial by-eye strip, $N_{\text{jit}} = 500$ random “jitter” experiments are run, where each jitter

1. Multiplies the provisional slope m_0 by $1 + \delta$ with $\delta \sim \mathcal{N}(0, 0.30^2)$ ($\pm 30\%$) scatter.
2. Re-anchors the line so it passes through the midpoint $(\frac{1}{2}(x_1 + x_2), \frac{1}{2}(y_1 + y_2))$.
3. Re-selects stars within the same gap g and fit a weighted least-squares slope $m_{\text{jit}}^{(k)}$.

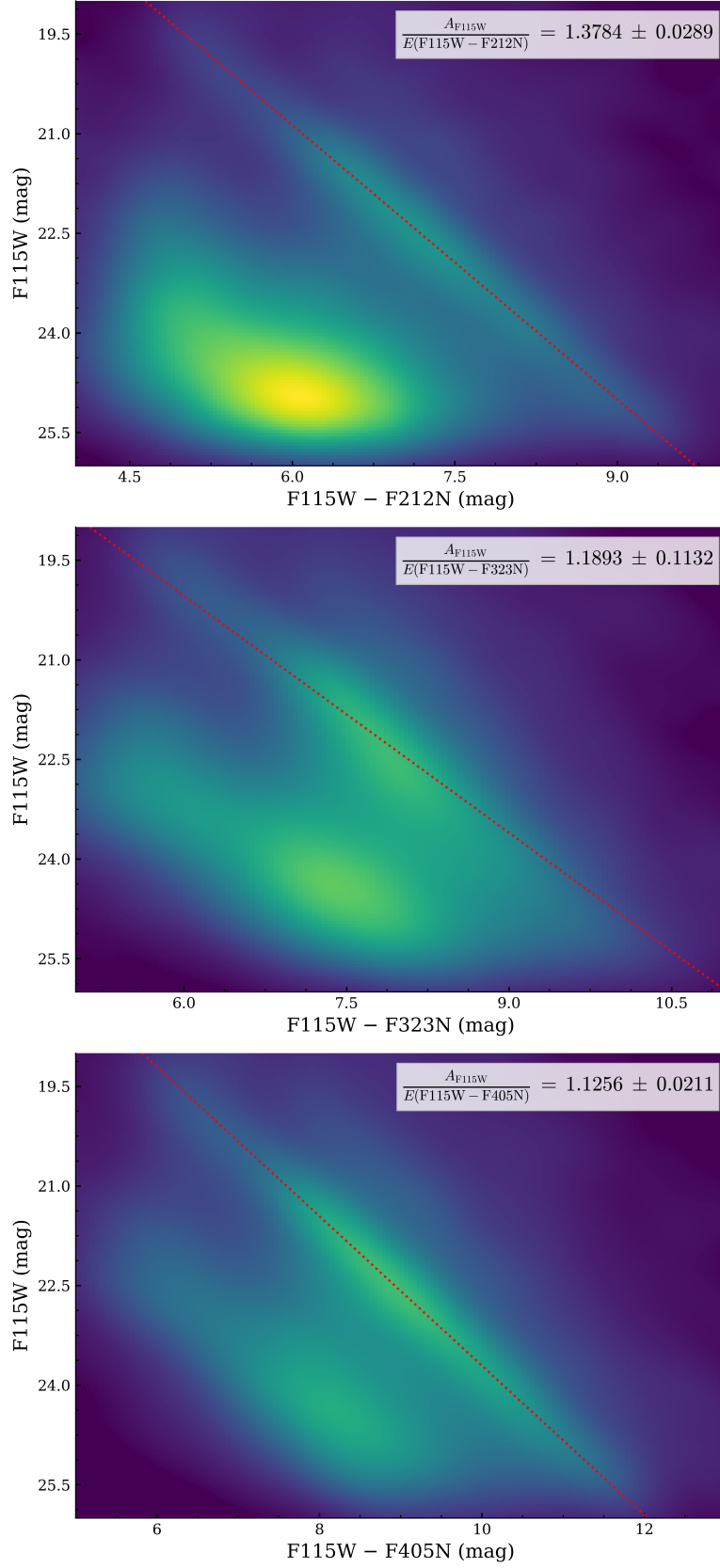
If at least two jitters succeed, their sample standard deviation

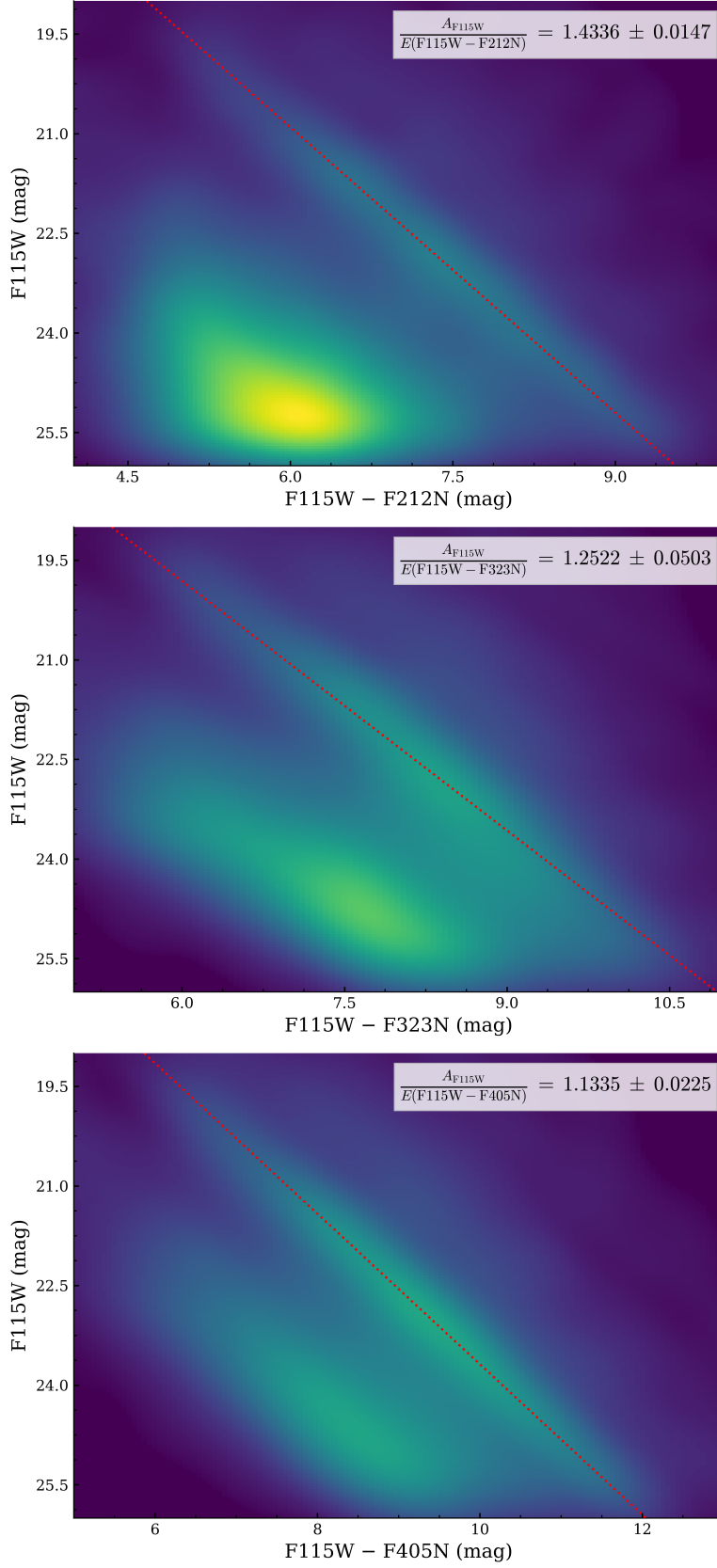
$$\sigma_{\hat{m}, \text{sys}} = \sqrt{\frac{1}{N_{\text{jit}} - 1} \sum_k (m_{\text{jit}}^{(k)} - \bar{m}_{\text{jit}})^2},$$

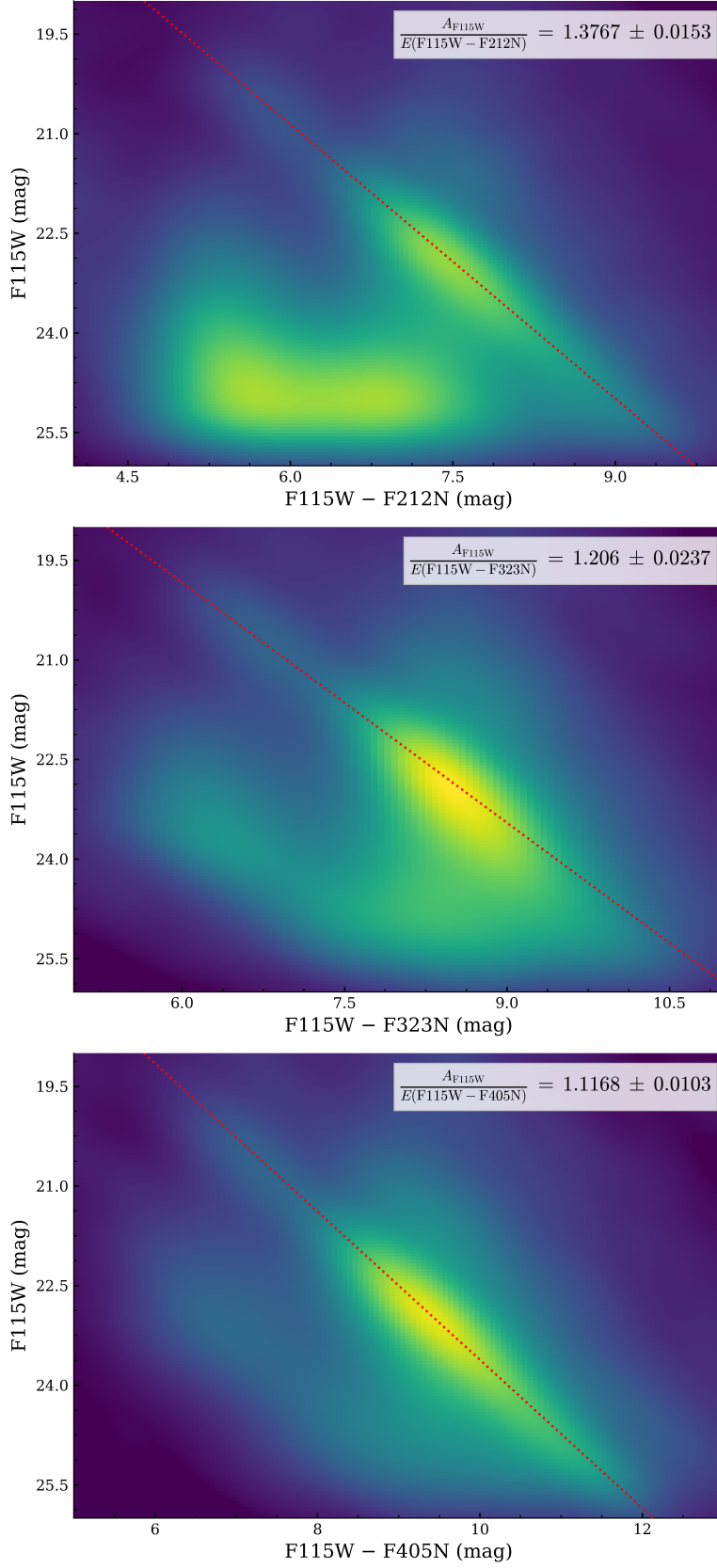
is taken as the systematic uncertainty due to the initial ansatz strip. The final slope measurement is therefore

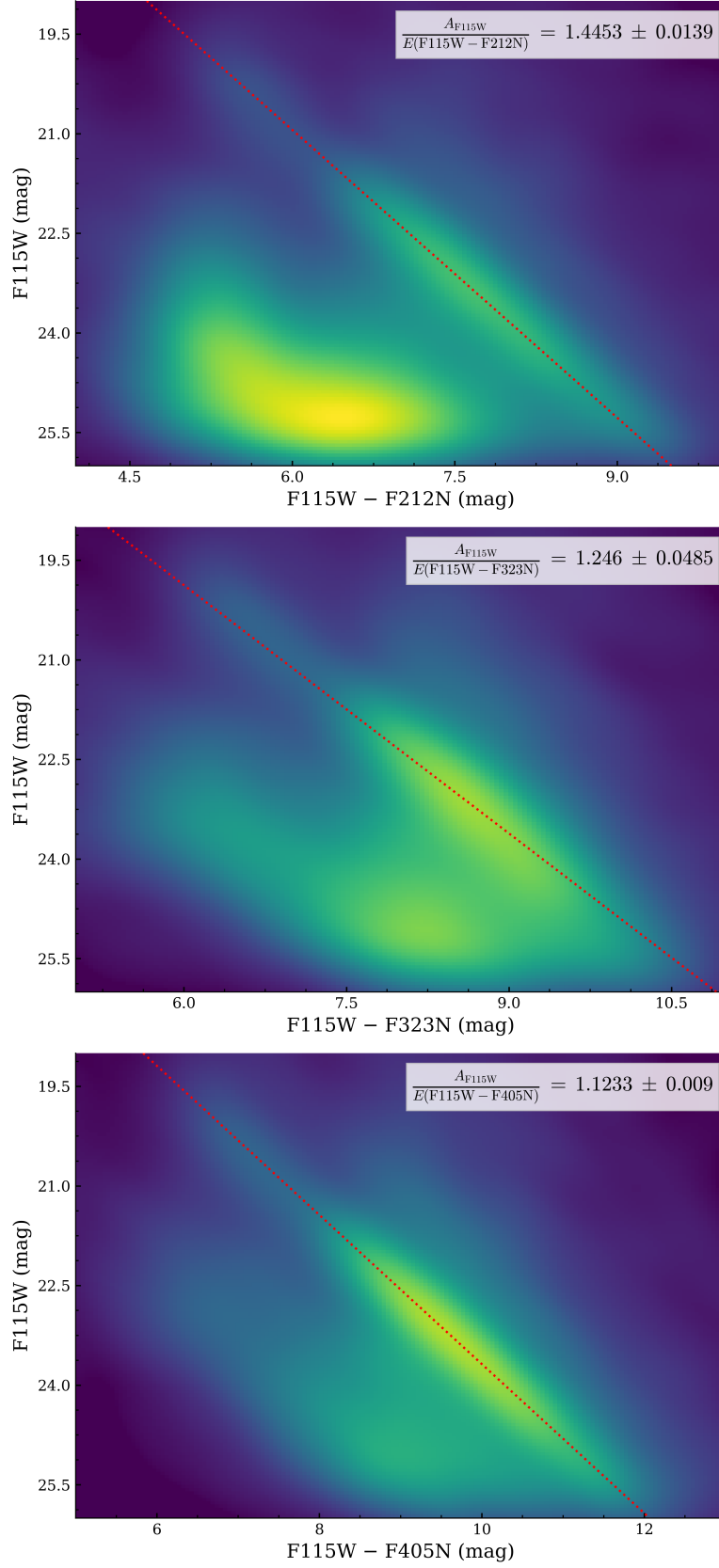
$$\hat{m} \pm \sigma_{\hat{m}}, \quad \sigma_{\hat{m}} = \sqrt{\sigma_{\hat{m}, \text{stat}}^2 + \sigma_{\hat{m}, \text{sys}}^2}.$$

For all NRCB footprints in the F115W – F323N vs. F115W CMDs, the 1σ confidence intervals from Method 1 and Method 2 overlap, indicating consistency (Table 4). However, only the slope estimates from Method 1 are used for the extinction ratio calculations. The following Figures 4–15 display all NRCB1–4 CMDs that were analyzed in this study with their calculated RC slopes that gave the total-to-selective extinction ratios $A_{F115W}/E(F115W - \lambda)$ for $\lambda \in \{F115W, F323N, F405N\}$.

**Figure 12.** NRCB1

**Figure 13.** NRCB2

**Figure 14.** NRCB3

**Figure 15.** NRCB4